Spin and Valley Filter Based on Two-Dimensional WSe_2 Heterostructures

D. Zambrano,[1] P.A. Orellana,[1] L. Rosales,[1] and A. Latgé[2,*]

[1] *Departamento de Física, Universidad Técnica Federico Santa María, Casilla 110-V, Valparaíso, Chile*
[2] *Instituto de Física, Universidade Federal Fluminense, Niterói-RJ, Brazil*

(Received 5 January 2021; revised 25 February 2021; accepted 9 March 2021; published 24 March 2021)

In this work, we investigate the spin and valley transport properties of a WSe_2 monolayer placed on top of a ferromagnetic insulator. We are interested in controlling the transport properties by applying external potentials to the system. To obtain spin and valley polarizations, we consider a single- and a double-barrier structure with gate potentials. We analyze how the efficiency of these polarized transport properties depends on the gate-potential intensities and geometrical configurations. Additionally, we investigate how the spin and valley transport properties are modified when an ac potential is applied to the system. We obtain a controllable modulation of the spin and valley polarizations as a function of the intensity and frequency of the ac potential, mainly in the terahertz range. These results validate the proposal of double quantum well structures of WSe_2 as candidates to provide spin- and valley-dependent transport within an optimal geometrical parameter regime.

DOI: 10.1103/PhysRevApplied.15.034069

I. INTRODUCTION

Transition-metal dichalcogenides (TMDCs) play an important role in nanotechnology nowadays due to their novel physical and chemical properties [1–8]. Compared with graphene, they have the great advantage of presenting electronic gaps in a wide size range within the visible and infrared spectra. Examples of TMDCs are tungsten disulfide (WS_2), molybdenum diselenide ($MoSe_2$), tungsten diselenide (WSe_2), and molybdenum disulfide (MoS_2) [9–18]. These materials have been considered for many technological applications in electronics [19,20] and optoelectronics [21–23], as gas-sensing [24] devices and ultrasensitive photodetectors [25], among others [9–12,26,27]. In particular, the TMDC monolayer of group VI presents a direct band gap in the optical range, suggesting possible applications in optoelectronics devices. In this context, TMDCs have emerged as excellent candidates for ultrathin semiconductor materials, with a tunable band gap in the optical region [6,19]. Moreover, the application of appropriate gate voltages and the presence of magnetic materials to induce magnetic proximity effects have been explored, revealing the different mechanisms of tailoring the electronic properties [28].

The electronic transport properties of TMDCs and their possible applications are determined by the corresponding carrier mobility and the mean free path of the spin and valley carriers [7]. There are several challenging proposals that involve the possibility of spin and valley filtering within spintronic and valleytronic scenarios [29] The theoretically predicted values for the charge mobility are promising but, of course, limited by intrinsic scattering processes such as phonon scattering or local Coulomb potentials induced by impurities [5–8,19]. Besides, spin-orbit coupling induced valley Hall effects have been reported on TMD materials and addressed as a manifestation of the applied gate voltage [30]. This type of induced valley Hall effect has been attributed to the coexistence of Ising and Rashba spin-orbit coupling in gated and/or polar TMDCs originating from inversion-asymmetric spin-orbit interactions.

Although most of the studies on transport properties of TMDC systems have been made in the *dc* regime, interesting quantum transport phenomena appear when external time-dependent fields perturb these materials. Comparing with stationary potentials, a time-varying one can effectively modulate the quantum phase of the electronic wave functions [31–33], yielding new possibilities for technological devices. Single-electron pumps have been designed applying a time-dependent gate voltage in quantum systems [34] and radio-frequency analog electronic devices have been synthesized based on carbon nanotube (CNT) transistors [35]. Other interesting effects are the photon-assisted tunneling in graphene bilayers [36], *ac*-field effects on the conductance and noise of CNT and graphene nanoribbon devices in the Fabry-Perot regime [37,38], quantum charge pumping in carbon-based devices [39], and irradiated graphene as a tunable Floquet topological insulator [40].

*alatge@id.uff.br

In TMDCs, the photon-assisted transport response has been less reported in comparison with other materials. For instance, the electric behavior of a mechanically exfoliated MoS_2 single-layer-based phototransistor [41] has been investigated. The photocurrent generation has been found to depend solely on the illuminating optical power at a constant drain or gate voltage, exhibiting better photoresponsivities than those proposed in the graphene-based device. Hybrid TMDC photoelectronic devices, based on graphene-MoS_2, have been proposed [42] as a possible application in multifunctional photoresponsive memory devices. Also, a photocurrent has been found at zero bias voltage [43] in an p-n vertical junction formed by a hybrid system of WSe_2 and MoS_2, as the system is irradiated by a 514-nm laser (5 μW). Studies of the influence of an optical field on spin- and valley-polarized transport of WSe_2 monolayer have recently been reported also taking into account the effects of a Fermi-velocity barrier [44]. All these reports undoubtedly suggest that photon-assisted phenomena can be an additional mechanism of controlling transport in TMDC nanostructures.

With the above motivations, here we investigate the possibility of inducing and controlling spin and valley polarizations on different potential profiles of two-dimensional (2D) WSe_2 heterostructures. We study the case of single- and double-potential-barrier configurations. We focus on the resonant regime and how this effect allows the spin and valley polarizations. Exchange valley splitting is provided by the magnetic proximity effect, with the advantages that the splitting is dictated by the exchange interaction strength and that no applied magnetic field is required. This allows a convenient scenario for obtaining the tuning processes. Moreover, due to the versatility of being either positive or negative valued, this description opens up the possibility of tuning the valley splitting sign and magnitude together. Furthermore, we analyze the possibility of promoting valley and spin polarization inversions on TMDC layers under the effects of time-dependent external potentials, such as time-oscillating gate voltages or laser irradiation. Different mechanisms are analyzed to synchronize the physical parameters of the proposed system, such as the Fermi energy, the frequency and amplitude of the time-dependent potential, and the external gate voltages, to optimize the time-dependent transport properties, such as the induced switching effects of the transport of the systems.

II. THE MODEL

The proposed device consists of a WSe_2 monolayer partially placed over a ferromagnetic insulator (EuS), as schematically depicted in Fig. 1. The whole system is composed of three regions: two leads, modeled by pristine regions of WSe_2, and a central conductor at which a ferromagnetic insulator is fixed under the WSe_2 layer.

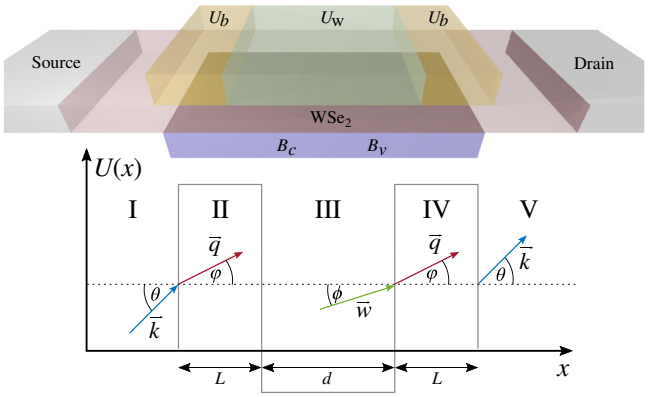

FIG. 1. A schematic view of a WSe_2 double-barrier heterostructure. Zones II and IV are the potential barriers of length L and height U_b. Region III is the well, with length d and depth U_w. In zones II, III, and IV, the presence of the substrate provides the exchange potentials B_c and B_v.

In order to modulate the transport response of the system, we consider top-gate potentials in different configurations, forming two distinct heterostructures: (i) a single barrier and (b) a double barrier. In the case of the single barrier, a top gate is placed over the finite region of the central conductor, whereas for the double-barrier configuration, three different top gates are used to define this system, as marked in yellow and green in Fig. 1.

The Hamiltonian describing the 2D system of interest can be written as

$$H = H_0 + H_{\rm ex} + H_g + H_{\rm ac}, \tag{1}$$

where H_0 is an effective Hamiltonian, written in the continuum model as discussed in previous works [1,2], which adjusts well with density-functional theory (DFT) calculations. This is a convenient approach to study transport response near the Fermi energy. The term $H_{\rm ex}$ represents the exchange field induced by the interaction of the WSe_2 layer with the EuS ferromagnetic insulator, which promotes an energy-exchange splitting as a magnetic proximity effect. The last two terms correspond to an external gate voltage H_g that can spatially modulate tunneling and resonance features, while $H_{\rm ac}$ is a time-dependent potential.

In the low-energy approximation, the effective Hamiltonian is written as

$$H_0 = v_F\left(\eta\sigma_x p_x + \sigma_y p_y\right) + \frac{m}{2}\sigma_z + \eta S_z\left(\lambda_c\sigma_+ + \lambda_v\sigma_-\right), \tag{2}$$

where v_F is the electronic Fermi velocity and $\eta = \pm 1$ refers to K and K' valleys. The second term is the mass term, which breaks the inversion symmetry, and $S_z = \pm 1$ is the spin index. The parameters $\lambda_{c,v}$ give the spin splitting

of the conduction and valence bands, respectively, and are due to intrinsic spin-orbit coupling, and

$$\sigma_{\pm}=\frac{1}{2}\left(\sigma_0 \pm \sigma_z\right), \tag{3}$$

with σ_0 denoting the identity matrix. Following Norden *et al.* [1] and Qi *et al.* [2], the exchange term is written as

$$H_{\rm ex} = -S_z\left(B_c\sigma_+ + B_v\sigma_-\right), \tag{4}$$

where $B_{c,v}$ may be interpreted as an effective Zeeman field experienced by the conduction and valence bands of the WSe_2 due to the proximity to the ferromagnetic substrate. It is important to mention that the Norden-model parameters are based on DFT calculations to reproduce the exact band structures of WSe_2 in the low-energy regime.

The external-gate-voltage term is defined as

$$H_g = U(x), \tag{5}$$

where $U(x)$ represents a sequence of potential barriers and wells that define a heterostructure device, as illustrated schematically in Fig. 1, for the case of a double-barrier system. We have denoted the barrier length as L and the potential barrier height as U_b, whereas the well length is taken as d and the potential well deep is given by U_w. Finally, the time-dependent Hamiltonian term is given by $H_{\rm ac} = eV(t) = V_{\rm bias}\cos(\omega t)$, where $V_{\rm bias}$ and ω represent the ac-potential intensity and the frequency, respectively. It is important to mention that, following the Tien-Gordon approach [45], this term has been applied to the whole system.

In our model, we do not include the Rashba interaction in the Hamiltonian, because we consider the exchange coupling more relevant in our approach. In the calculation, we are interested in the electronic transport through the conduction band that presents an energy splitting greater than the usual Rashba term [30].

We consider the cases of a single-barrier and a double-barrier potential profile. The electronic transmission through the conductor region is calculated following the same scheme, in both configurations, as described in the Appendix. The transmission coefficient of the single barrier, $t^{\rm single}_{\eta,S_z}$, can be analytically determined, and is given by

$$t^{\rm Single}_{S_z,\eta} = \frac{2}{\xi}\cos(\theta)\cos(\varphi)\,e^{-ik_xL}, \tag{6}$$

where the term ξ is defined as

$$\xi = \cos(\theta-\varphi)\,e^{iq_xL} + \cos(\theta+\varphi)\,e^{-iq_xL} - i\left(\frac{c_kb_q}{c_qb_k}+\frac{c_qb_k}{c_kb_q}\right)\sin(q_xL), \tag{7}$$

where $\theta = \arctan(k_y/k_x)$, $\varphi = \arctan(k_y/q_x)$, $k_{x,y}$, and $q_{x,y}$ are the wave-vector components of the electron outside and inside the barrier, respectively, and c_k, c_q, b_k, and b_q are the amplitude coefficients of the electronic wave function outside and inside the barrier, defined in the Appendix. It is also possible to obtain an analytic expression for the double-barrier transmission coefficient $t^{\rm Double}_{S_z,\eta}$, which is derived in the Appendix in Eq. (A16).

For both cases ($t^{\rm Single}_{S_z,\eta}$ and $t^{\rm Double}_{S_z,\eta}$), the angle-dependent transmission probability $T_{S_z,\eta}(\theta)$ is defined as

$$T_{S_z,\eta}(\theta) = \left|t_{S_z,\eta}\right|^2, \tag{8}$$

while the spin and valley conductances are written as

$$\mathcal{G}_{S_z,\eta} = \int_{-\pi/2}^{\pi/2} T_{S_z,\eta}\cos(\theta)d\theta. \tag{9}$$

We discuss further the effects of an ac potential of frequency ω and intensity $V_{\rm ac}$ on the transport properties of the proposed device. Following the Tien-Gordon formalism [45], the spin and valley conductances may be written as [36]

$$G_{S_z,\eta} = G_0\sum_{m=-\infty}^{\infty} J_m^2\left(\frac{eV_{\rm ac}}{\hbar\omega}\right)\mathcal{G}_{S_z,\eta}(\varepsilon_f + m\hbar\omega), \tag{10}$$

where the J_m are Bessel functions of first kind.

Here, we use the spin-dependent conductance as

$$G_{\uparrow(\downarrow)} = G_{\uparrow(\downarrow)K} + G_{\uparrow(\downarrow)K'} \tag{11}$$

and the valley-dependent conductance as

$$G_{K(')} = G_{\uparrow K(')} + G_{\downarrow K(')}. \tag{12}$$

Following standard definitions, the valley-polarized conductance is written as

$$P_v = \frac{G_K - G_{K'}}{G_K + G_{K'}}, \tag{13}$$

whereas the spin-polarized conductance is written as

$$P_S = \frac{G_\uparrow - G_\downarrow}{G_\uparrow + G_\downarrow}. \tag{14}$$

In what follows, we discuss the results for spin and valley polarizations obtained for both single- and double-barrier heterostructure systems, considering different mechanisms to modulate the transport response of the proposed device.

III. RESULTS

The low-energy band structures for the WSe_2 heterostructure are presented in Fig. 2, considering the three regions: leads, barriers, and the well. For simplicity, we adopt the notation of K_+ and K_-, for the traditional K and K' valleys. The red and blue curves denote the spin-up and spin-down bands that, due to the symmetries of WSe_2, are inverted for the K_+ and K_- valleys. To obtain these band structures, we use the following parameter values: $\lambda_c = 34.20$ meV, $\lambda_v = 418.05$ meV, $B_c = 18.20$ meV, $B_v = 13.75$ meV, and $m = 1558.70$ meV [1]. The lattice constant is $a_0 = 0.3316$ nm and the Fermi velocity $v_f = 5.30 \times 10^{14}$ nm/s.

The energy split induced by the ferromagnetic substrate (B_c and B_v) for the well and barrier regions is marked with dashed black lines in the electronic band structures presented in Figs. 2(b) and 2(c). The energy split $\Delta E = 36.40$ meV matches those reported in Fig. 7 of Ref. [1]. The energy axis is redefined as $E - E_{\text{bott}}$, where $E_{\text{bott}} = 745.15$ meV is the bottom energy of the conduction bands in the leads. The horizontal black lines in the three panels of Fig. 2 represent the incoming-electron energy level, which is 104.68 meV (175.10 meV) above the Fermi level for the double- (single-) barrier system. Energy values up to 400 meV are considered for the potential U_b of the double-barrier system and are chosen in a symmetric configuration. In the case of the single-barrier system, U_b takes values up to 200 meV. For the well potential U_w, values up to 100 meV are considered. In this context, it is possible to observe in Figs. 2(b) and 2(c) how the spin bands are displaced as the potentials U_b and U_w are applied in the system.

We discuss first the cases of single- and double-barrier heterostructures in the absence of the time-dependent term, presented in Eq. (A8). The ac-field contribution is only taken into account in Sec. III C, where a double-barrier system is revisited under the effects of a time-dependent radiation.

A. Single barrier

The results of spin- and valley-resolved conductance and polarization, as a function of the single-barrier potential energy, are presented in Figs. 3(a) and 3(b). Here, we choose a barrier length $L = 20$ nm and an incident electron energy $E = 175.10$ meV above the Fermi level. The four spin- and valley-conductance components are denoted as $\uparrow K_+$ and $\downarrow K_+$ for the valley K_+ and as $\uparrow K_-$ and $\downarrow K_-$ for the valley K_-. All of the conductance curves fall, as expected, as the barrier height increases, blocking the electronic transport. The corresponding spin and valley polarizations, given by the blue and red curves, respectively, depend strongly on the barrier height, as shown in Fig. 3(b). It is important to note that the polarization is not very pronounced when the four conduction channels are active, mainly the valley polarization. However, as the conductance starts to decrease, the polarization is enhanced, achieving maximum values when there is just a single conduction channel [the green curve in Fig. 3(a)]. Particular potential values ($0.16 < U_b < 0.20$) predict the total polarized spin and valley configurations. A full spin and valley filter can then be achieved in this single-barrier heterostructure.

We wonder how robust this spin and valley filter is as a function of the barrier length and the range of potential intensities that we use. In Fig. 4, we show contour plots of (a) the $\uparrow K_+$ and (b) the $\uparrow K_-$ conductance components, (c) the spin polarization P_s, and (d) the valley polarization as functions of the barrier height U_b and length L, at a fixed energy of 175.10 meV above the Fermi level. In Figs. 4(a) and 4(b), it is possible to observe that the $\uparrow K_+$ and $\uparrow K_-$

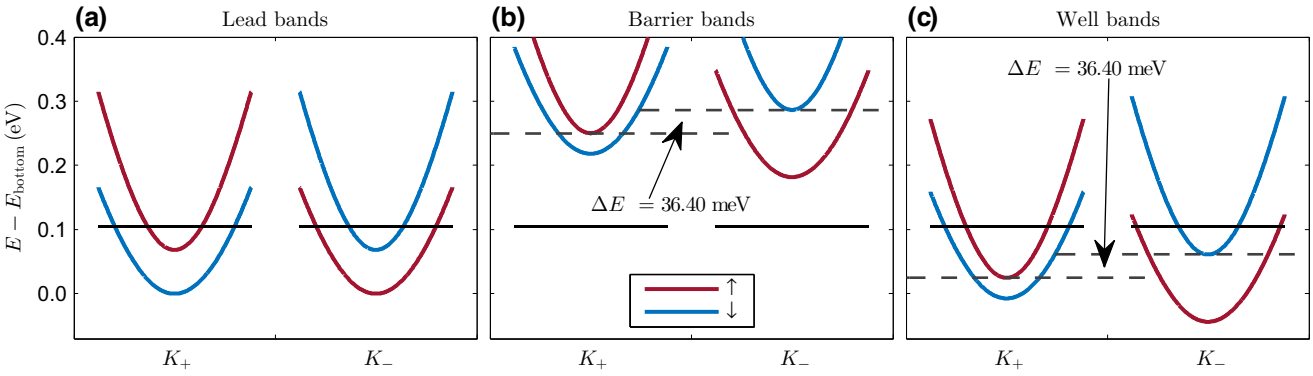

FIG. 2. The band structures of a WSe_2 heterostructure corresponding to (a) the leads, (b) the barrier region, and (c) the well region, composed of a double-barrier system [in a single-barrier system, panel (c) is neglected]. The bottom of the lead conduction band has been redefined as zero energy. The solid black lines show the energy of the incoming electrons. The dashed black lines in (b) and (c) define the energy difference between the bottom of the spin-up conduction band in the valley K_+, and the spin-down conduction band in the valley K_-.

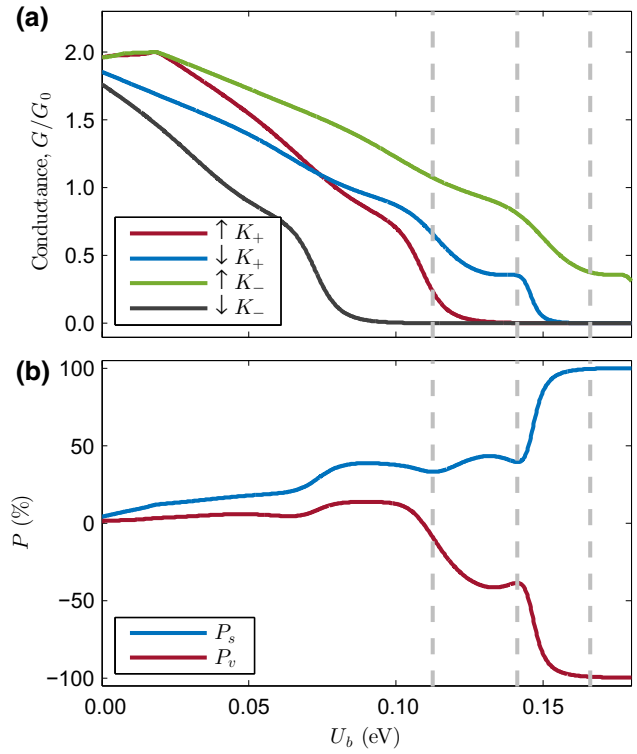

FIG. 3. The spin and valley conductances (a) and polarizations (b) as a function of the barrier height U_b for the single-barrier system, with barrier length $L = 20$ nm. Both panels are at energy 175.10 meV above the Fermi level.

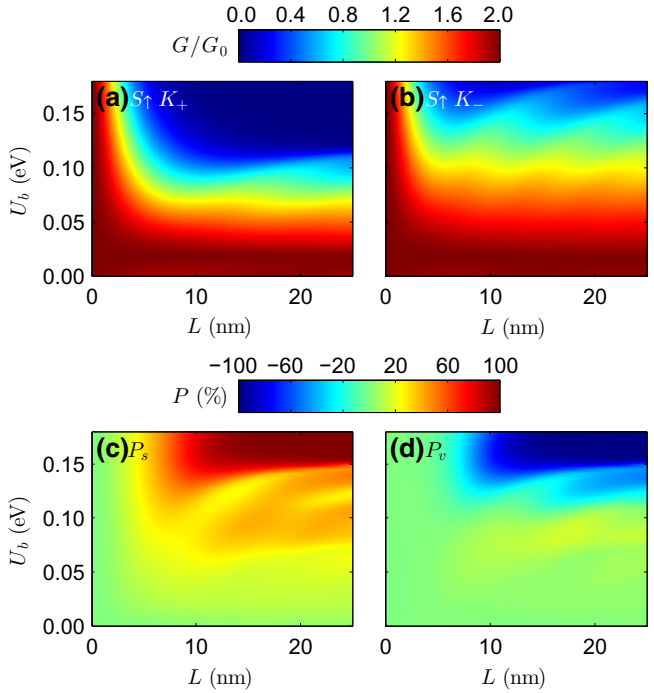

FIG. 4. (a) The $S \uparrow K_+$ conductance component, (b) the $S \uparrow K_-$ conductance component, and (c) the spin- and (d) the valley-polarization contour plots, for a single-barrier system, as functions of the barrier height U_b and length L, at a fixed energy of 175.10 meV above the Fermi level.

conductance components behave uniformly as the barrier length is increased over 5 nm, their values diminishing as the potential intensity U_b becomes higher. However, there is a different potential intensity at which these two components become zero, around 0.1 eV for $\uparrow K_+$ and 0.15 eV for $\uparrow K_-$, respectively. Considering Eqs. (14) and (13), it is possible to obtain perfect spin and valley filters over a wide range of parameters, as reflected in Figs. 4(c) and 4(d). Thus, single-barrier heterostructures larger than 10 nm and with a potential energy range between 140 and 200 meV are appropriate to obtain spin and valley filters, as indicated by the red and blue regions in both polarization contour plots. These results provide guidelines for the choice of single-barrier WSe_2 heterostructures that would behave as a filter.

B. Double barrier

In what follows, we explore different configurations for the top-gate voltages applied to the WSe_2 monolayer that transform the system into semiconducting quantum well heterostructures. The results for the spin and valley conductances and polarizations as a function of the well potential energy are shown in Figs. 5 and 7 for a symmetric double-barrier device. The left and right barrier lengths and potentials are equal to $L = 3$ nm and $U_b = 300$ meV, respectively. Although apparently small, such a size of barrier corresponds to around ten atomic layers, which is experimentally feasible nowadays [46]. The well length is fixed and equal to $d = 30$ nm. Unlike the tunneling phenomena observed in the single-barrier case, resonant states are typical for double-barrier profiles, which define the transport behavior of this kind of resonant system. The states may be tuned, for instance, by changing the well potential depth. This is evidenced in the sequence of conductance peaks depicted in Fig. 5(a). The features of the spin and valley components of the conductance are similar, although shifted in relation to the potential depth. This is understood by the alignment of the allowed conduction channels inside of the well region (defined by the well length) and the incident electron energy, as the potential U_w is modified (see Fig. 2).

It is important to note that the conductance peak values associated with the resonant states do not attain their maxima. The presence of evanescent states and energy-level changes due to the exchange coupling may be some of the reasons. Another important contribution comes from the angular dependence of the transmission, as illustrated in Figs. 5(b) and 5(c). Partial maximum conductance values at particular values of U_w denoted by dashed lines in Fig. 5(a) do exhibit maximum transmission but are restricted to a finite angular range, as explicitly shown in

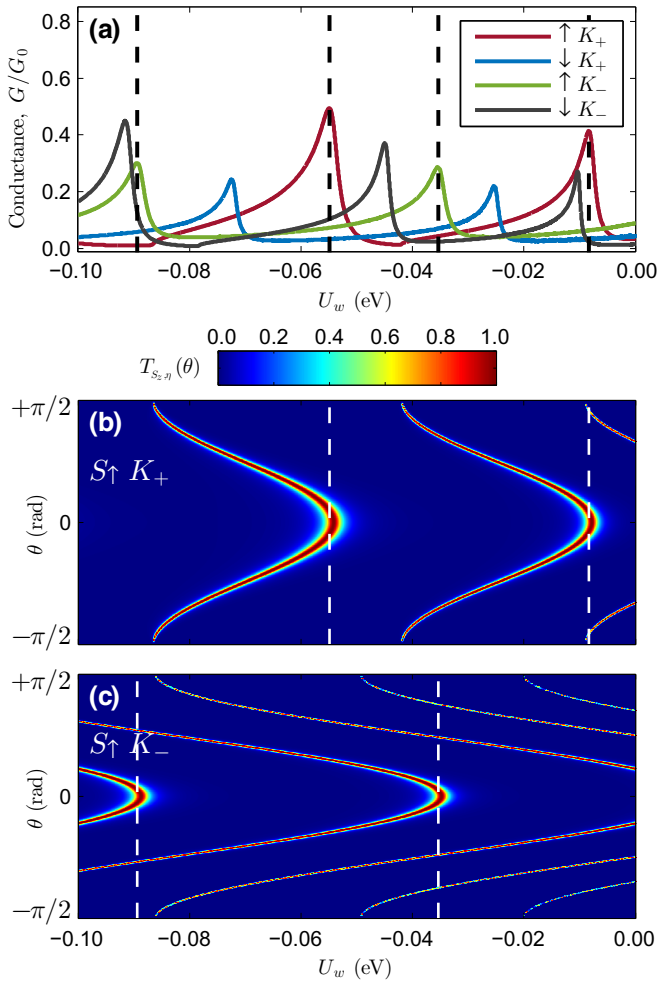

FIG. 5. (a) The spin and valley conductances as a function of the well depth for a double-barrier system: barrier length $L = 3$ nm, well length $d = 30$ nm, and barrier height $U_b = 300$ meV. (b),(c) The transmission as a function of the incident angle θ. The white dashed lines correspond to the peaks of the conductance components, shown in (a) with black dashed lines. All panels are at 104.68 meV above the Fermi level.

Figs. 5(b) and 5(c), leading to a lower conductance that is less than one quantum conductance. In fact, we can also observe that the transmission probability takes high values for angles around the normal incidence of the carriers. The sequence of conductance peaks allows a rich variety of spin- and valley-polarization dependencies on the well depth, as shown in Fig. 5(b), which may be explored.

The band alignments of the leads and well, and the transmission for the spin-up bands K_+ and K_- bands, shown in Fig. 6, help in understanding the resonant features of the conductance and polarization results. The transmission for each band is shifted due to the presence of the EuS substrate. The transmission maxima are highlighted with dot symbols in the well bands, as depicted in Figs. 6(a) and 6(b). For normal incidence, as the gate potential is applied in the central region, the resonant levels (dots) begin to align with the Fermi energy at the leads (marked with a black horizontal line) and, as a consequence, the conductance exhibits a series of sharp and well-defined peaks. As expected, the number and energy distribution of these peaks depend on the well-region length, which is a favorable condition to obtain gate-tunable values of spin and valley polarization. It is important to emphasize that the perfect resonant conductance peaks observed in Fig. 6 are obtained only for normal incidence; otherwise, an angle-integrated conductance value has to be calculated [via Eq. (9)], giving broad peaks centered at the resonant energy values. These resonances can be tuned by the gate potentials, generating the corresponding spin- and valley-transport polarizations.

Two relevant situations for the spin and valley polarization shown in Fig. 7 are highlighted with dashed lines in this plot: (i) a potential at which both the spin and valley polarizations are zero (−85.9 meV) and (ii) a potential at which the valley and spin polarizations have opposite signs (−25.4 meV). We investigate how these polarizations depend on the barrier length L and on the potential height U_b, at both energies, as depicted in Figs. 8(a)–8(d). In the contour plots, $U_w = -25.4$ meV and -85.9 meV for top and bottom panels, respectively. The results suggest that it is possible to obtain zero polarization or a highly spin- and valley-polarized heterostructure depending on the potential well energy, over a wide range of parameter space (U_b, L). It is also observed that by increasing the barrier potential intensity U_b, it is possible to change the spin and valley polarization signs, from positive to negative and vice versa, at a fixed barrier length, especially around $L = 4$ nm [see Figs. 8(a) and 8(d)]. As the barrier potential U_b is increased, the energy distribution of the resonant states in the well region changes, separating and defining these levels in such a way that the resonant tunneling is affected. For some U_b values, the system conducts preferentially by the $\uparrow K_+$ or the $\uparrow K_-$ conductance components promoting, therefore, a sign reversal of the spin and valley polarizations. Finally, for $d = 30$ nm, the optimal parameter space values (U_b, L) at which the maximum valley polarization is obtained are around $U_b = 200$ meV and $L > 2.5$ nm.

We further explore the dependence of the valley and spin conductances and polarizations on the quantum well potential U_w and length d. The results for each of the conductance components, for a double-barrier system of length and height $L = 3$ nm and $U_b = 300$ meV, respectively, and at a fixed incident electron energy $E = 104.68$ meV above the Fermi level, are presented in Figs. 9(a)–9(d). The resonant nature of the electronic states of the well are revealed through the paraboliclike features, marking nonzero conductance in the contour plots, as the intensity potential and geometrical dimension of the quantum well are swept. The spin and valley polarization contour plots, depicted in Figs. 9(e) and 9(f), respectively, present complex patterns,

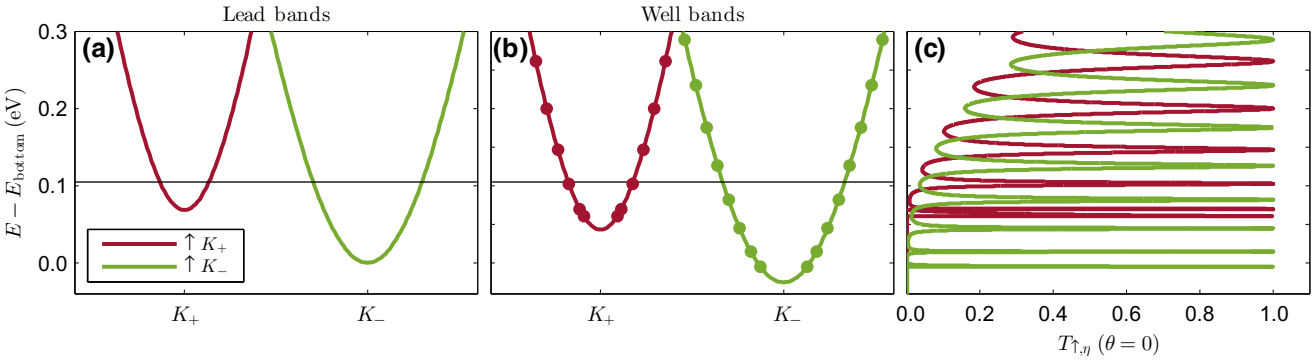

FIG. 6. (a),(b) The lead and well bands (spin up), for the case of a double-barrier system with barrier and well lengths $L = 3$ nm and $d = 30$ nm, respectively, barrier height $U_b = 300$ meV, and well depth $U_w = -25.40$ meV. The energy of the incoming electrons, chosen as 104.68 meV above the Fermi level, is marked as black horizontal lines. (c) The spin-valley transmission as a function of the incoming-electron energy for the double-barrier system, in the case of normal incident angle $\theta = 0$.

clearly indicating that drastic changes may occur for a fixed quantum well length as the well potential goes from zero to -100 meV. It is important to note that, to avoid spurious results, in these plots we calculate the weighted polarization [36,47], which is defined as $wPS = G_{\uparrow(\downarrow)}P_S$ and $wP_v = G_{K(')}P_v$.

C. External ac field

As previously mentioned, we address the possibilities of obtaining interesting spin and valley filter scenarios for WSe_2 devices by properly exposing the system to a time-dependent radiation. The external potential can be a laser or a time-dependent gate voltage, with frequency $\hbar\omega$ and amplitude potential eV_{ac}, applied to the whole system. In order to obtain modulations of the heterostructure transport response, we explore different time-dependent potential parameters ($\hbar\omega$, eV_{ac}). The main features obtained for a double-barrier device, under the oscillating potential, are illustrated in Fig. 10 via spin and valley conductance [(a) and (b)] and polarization [(c)–(f)] contour plots in the midinfrared (between 413 and 24.8 meV) and the far infrared or terahertz (between 24.84 and 1.24 meV) frequency range, and as a function of the amplitude potential eV_{ac}. The analyzed structure has a barrier height $U_b = 300$ meV and length $L = 3$ nm, whereas the quantum well geometry is defined by a well length $d = 30$ nm and two potential depths $U_w = -25.40$ meV and -85.90 meV, in the left and right panels, respectively. These potential values are marked with dashed white lines in the

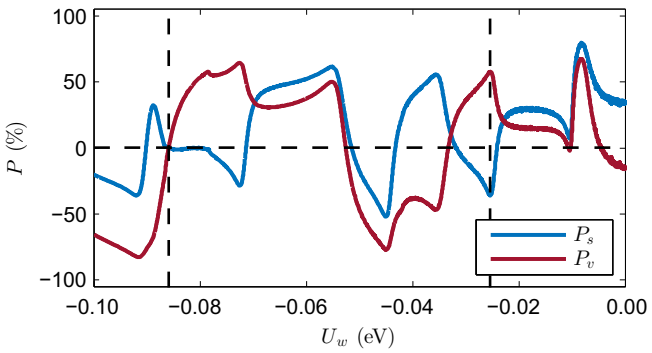

FIG. 7. The spin and valley polarizations as a function of the well depth for the double-barrier system: barrier length $L = 3$ nm, well length $d = 30$ nm, and barrier height $U_b = 300$ meV at 104.68 meV above the Fermi level. The vertical dashed lines are drawn at $U_w = -85.9$ meV and at -25.4 meV.

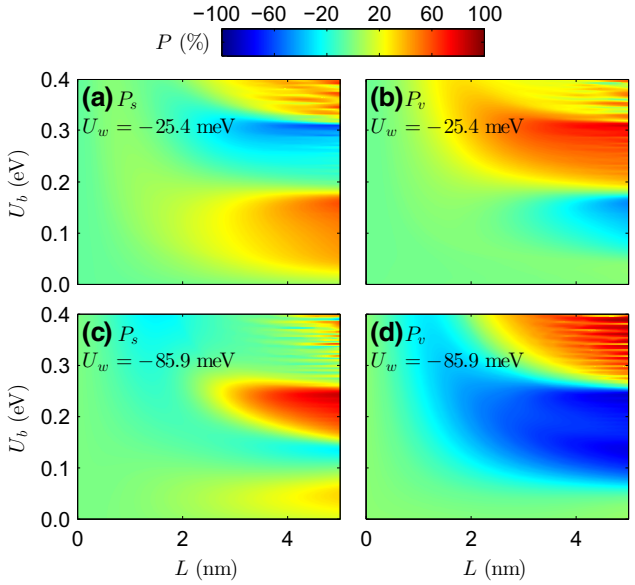

FIG. 8. The spin- and valley-polarization contour plots as functions of the barrier height U_b and length L for the double-barrier system at a fixed energy equal to 104.68 meV above the Fermi level. The well length is $d = 30$ nm; the well depth for (a) and (b) is $U_w = -25.40$ meV, while for (c) and (d) it is $U_w = -85.90$ meV.

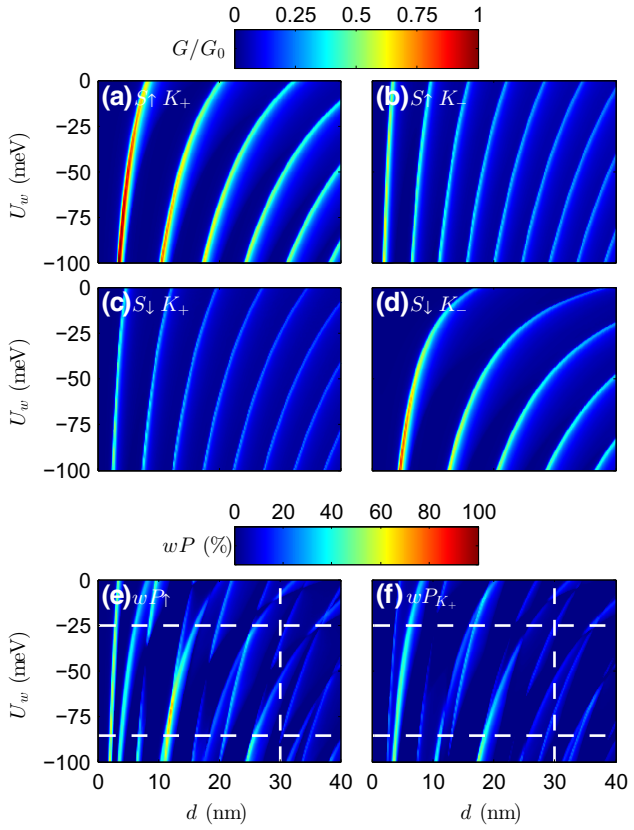

FIG. 9. The spin and valley conductance (a)–(d) and weighted polarization contour plots (e),(f) as functions of the well depth and length, U_w and d, for the double-barrier system at a fixed energy of 104.68 meV above the Fermi level. The barrier length and height are $L = 3$ nm and $U_b = 300$ meV, respectively.

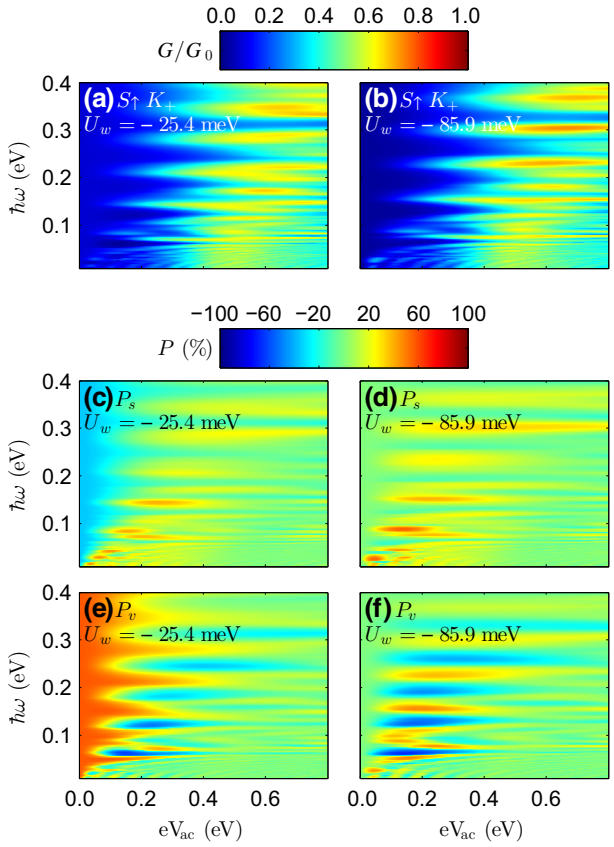

FIG. 10. The spin and valley conductance and polarization contour plots as functions of the ac-field frequency $\hbar\omega$ and power eV_{ac}, for the double-barrier system in the far-infrared frequency range: barrier and well lengths $L = 3$ nm and $d = 30$ nm, barrier height $U_b = 300$ meV. The well depths for the left (a),(c),(e) and right (b),(d),(f) panels are $U_w = -25.4$ meV and $U_w = -85.9$ meV, respectively.

weighted-spin-polarization $\omega P_\uparrow$ and valley-polarization ωP_{K+} plots of Figs. 9(e) and 9(f).

The spin and valley resolved conductances [Figs. 10(a) and 10(b)] show that, by applying an oscillating potential to the system, with a radiation amplitude $0 < eV_{ac} < 0.8$ eV, both conductance components become different to zero, with an oscillating behavior as the frequency increases. This means that, due to the presence of the time-dependent ac field, the effective modulation of the electronic wave-function quantum phase promotes resonant tunneling in the double-barrier heterostructure. Actually, variations up to 70% are noted at particular potential amplitudes and frequencies.

Similar features are observed in the valley and spin polarization maps, considering the same two values of the potential well U_w, as depicted in the contour plots of Figs. 10(c)–10(f). For $U_w = -25.4$ meV and $U_w = -85.9$ meV, the spin polarization shows smooth and periodic modulations of its maximum value as the ac-field frequency is increased. However, there are narrow frequency ranges [orange regions in panels (c) and (d)] at which high spin polarization is observed, for different ac-field amplitudes. This is more evident for a deeper well potential ($U_w = -85.9$ meV), when more resonant states are allowed into the conductor region, and in the terahertz frequency range, up to 144 meV. For the valley polarization, at $U_w = -25.4$ meV, as the ac-field amplitude is turned on and increased, it is possible to switch from the K_+ to the K_- valley filter, as revealed by the sequence of orange and blue colors in the contour plots of panel (e), for a fixed ac-field frequency. Also, considering the potential well $U_w = -85.9$ meV, the system is moved from zero spin and valley polarizations to ±20% and ±60% spin and valley polarizations, respectively, depending on the far-infrared radiation frequency.

These valley-switch polarization features are highlighted in the enlargement presented in Figs. 11(a) and 11(b), where the laser frequency and potential amplitude are constrained in smaller ranges. Some 2D cuts for the valley and spin polarizations as a function of the ac-field amplitudes are presented in Figs. 11(c)–11(f), for fixed quantum well potential and frequency values, as

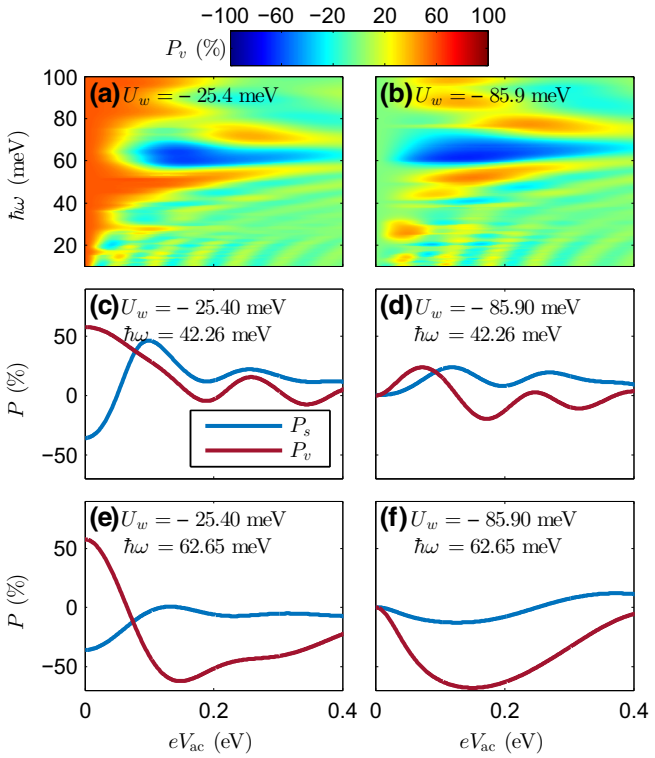

FIG. 11. (a),(b) Enlargements of the valley-polarization contour plots mapped in Figs. 10(e) and 10(f) for $U_w = -25.4$ meV and -85.9 meV, respectively. (c)–(f) Valley and spin polarization results as a function of the ac-field power for the same double-barrier system as described in the previous figure: barrier length $L = 3$ nm and height $U_b = 300$ meV, well length $d = 30$ nm. The well depths are $U_w = -25.40$ meV (left panels) and -85.90 meV (right panels). In all panels, $E_F = 849.98$ meV and the ac-field frequency $\hbar\omega = 42.26$ meV and 62.64 meV, as marked in each panel.

indicated in the panels. Actually, by adjusting the ac-field potential, a variety of filter regimes may be achieved, which transforms the double quantum well geometry into a promising platform to reveal the spin and valley filtering behavior of WSe_2 monolayers.

IV. SUMMARY

In this work, we investigate the spin and valley transport properties of a WSe_2 monolayer placed on top of a ferromagnetic insulator. Single- and double-barrier heterostructures are explored. By applying external potentials to the system, we show that the systems can be used as efficient valley and spin filter devices and how the polarized transport properties depend on the gate-potential intensities and the geometrical configuration. We believe that the combination of heterostructured TMD geometries and appropriated gate potentials, proposed in our work, allows us to control the resonant tuning provided by the state alignment with the electronic carrier bands. We find that double-barrier structures are more appropriate for valley and spin filters, due to the resonant tunneling, compared with single-barrier systems. Additionally, we investigate how the spin and valley polarizations are modified when an ac field is applied to the system. The radiation field allows the tuning of both polarizations over a wide range of device geometries, radiation intensities, and frequencies, especially in the terahertz range. Inversions of the spin and valley polarization signals are found to be possible by changing the laser frequency for fixed power amplitudes. The possibility of spin and valley polarization inversion may be considered as an advantage of our proposal. Our results suggest that 2D WSe_2 heterostructures are good candidates to provide spin- and valley-dependent transport and can drive experimental efforts in order to probe spin- and valley-polarized currents.

ACKNOWLEDGMENTS

This work was partially financed by the Fondo Nacional de Desarrollo Científico y Tecnológico (FONDECYT) of Chile, under Grants No. 1180914 and No. 1201876. A.L. would like to acknowledge partial support from the Fundação de Amparo à Pesquisa do Estado do Rio de Janeiro (FAPERJ) (Grant No. E-26/202.567/2019), the Conselho Nacional de Desenvolvimento Científico e Tecnológico (CNPq), and the Instituto Nacional de Ciência e Tecnologia (INCT) em Nanomateriais de Carbono.

APPENDIX

A Hamiltonian such as the one described by Eqs. (1), (2), (4), and (5) can always be written in the following form:

$$H = \begin{pmatrix} \Delta_c & \hbar v k_- \\ \hbar v k_+ & \Delta_v \end{pmatrix}. \tag{A1}$$

In our model, $\Delta_c = S_z(\eta\lambda_c + B_c) + U(x) + m/2$, $\Delta_v = S_z(\eta\lambda_v - B_v) + U(x) - m/2$, $k_\pm = \eta k_x \pm i k_y$, v is the Fermi velocity, and $\eta = \pm 1$ is the valley index. Note that $\hbar^2 v^2 k_+ k_- = (\hbar v k)^2 = c_k^2$.

A straightforward diagonalization of the low-energy Hamiltonian defined by Eq. (A1) leads to the following spinor for an incident electron in the conduction band:

$$V^{\eta}_{S_z,\pm} = \frac{1}{D_k}\begin{pmatrix} \eta c_k e^{-i\eta\theta} \\ b_k \end{pmatrix}, \tag{A2}$$

where $b_k = \sqrt{\Delta_-^2 + c_k^2} - \Delta_-$, $D_k = \sqrt{c_k^2 + b_k^2}$ and $2\Delta_- = \Delta_c - \Delta_v$.

Considering the invariance in the y direction and the structure shown in Fig. 1, the wave functions for the double-barrier system are

$$\Psi_{\rm I}(x,y) = \left[\frac{e^{ik_x x}}{D_k}\begin{pmatrix}\eta c_k e^{-i\eta\theta}\\ b_k\end{pmatrix} + r_{\eta,S_z}\frac{e^{-ik_x x}}{D_k}\begin{pmatrix}\eta c_k e^{-i\eta(\pi-\theta)}\\ b_k\end{pmatrix}\right]e^{ik_y y}, \tag{A3}$$

$$\Psi_{\rm II}(x,y) = \left[A\frac{e^{iq_x x}}{D_q}\begin{pmatrix}\eta c_q e^{-i\eta\varphi}\\ b_q\end{pmatrix} + B\frac{e^{-iq_x x}}{D_q}\begin{pmatrix}\eta c_q e^{-i\eta(\pi-\varphi)}\\ b_q\end{pmatrix}\right]e^{ik_y y}, \tag{A4}$$

$$\Psi_{\rm III}(x,y) = \left[C\frac{e^{iw_x x}}{D_w}\begin{pmatrix}\eta c_w e^{-i\eta\phi}\\ b_w\end{pmatrix} + D\frac{e^{-iw_x x}}{D_w}\begin{pmatrix}\eta c_w e^{-i\eta(\pi-\phi)}\\ b_w\end{pmatrix}\right]e^{ik_y y}, \tag{A5}$$

$$\Psi_{\rm IV}(x,y) = \left[E\frac{e^{iq_x x}}{D_q}\begin{pmatrix}\eta c_q e^{-i\eta\varphi}\\ b_q\end{pmatrix} + F\frac{e^{-iq_x x}}{D_q}\begin{pmatrix}\eta c_q e^{-i\eta(\pi-\varphi)}\\ b_q\end{pmatrix}\right]e^{ik_y y}, \tag{A6}$$

$$\Psi_{\rm V}(x,y) = t_{\eta,S_z}\frac{e^{ik_x x}}{D_k}\begin{pmatrix}\eta c_k e^{-i\eta\theta}\\ b_k\end{pmatrix}e^{ik_y y}, \tag{A7}$$

where the coefficients D_q, b_q, D_w, and b_w are defined in the same way as D_k and b_k, but with the corresponding parameters according to Fig. 1.

The transmission probability is found by matching the wave functions at the interfaces; at $x = 0$, we have $\Psi_{\rm I}(0) = \Psi_{\rm II}(0)$, which is written as two equations:

$$\frac{\eta c_k e^{-i\eta\theta}}{D_k} + r_{\eta,S_z}\frac{\eta c_k e^{-i\eta(\pi-\theta)}}{D_k} = A\frac{\eta c_q e^{-i\eta\varphi}}{D_q} + B\frac{\eta c_q e^{-i\eta(\pi-\varphi)}}{D_q}, \tag{A8}$$

$$\frac{b_k}{D_k} + r_{\eta,S_z}\frac{b_k}{D_k} = A\frac{b_q}{D_q} + B\frac{b_q}{D_q}. \tag{A9}$$

At $x = L$, we have $\Psi_{\rm II}(L) = \Psi_{\rm III}(L)$ and, similarly,

$$A\frac{\eta c_q e^{-i\eta\varphi}}{D_q}e^{iq_x L} + B\frac{\eta c_q e^{-i\eta(\pi-\varphi)}}{D_q}e^{-iq_x L} = C\frac{\eta c_w e^{-i\eta\phi}}{D_w}e^{iw_x L} + D\frac{\eta c_w e^{-i\eta(\pi-\phi)}}{D_w}e^{-iw_x L}, \tag{A10}$$

$$A\frac{b_q}{D_q}e^{iq_x L} + B\frac{b_q}{D_q}e^{-iq_x L} = C\frac{b_w}{D_w}e^{iw_x L} + D\frac{b_w}{D_w}e^{-iw_x L}. \tag{A11}$$

At $x = L + d$, $\Psi_{\rm III}(L+d) = \Psi_{\rm IV}(L+d)$ and we obtain

$$C\frac{\eta c_w e^{-i\eta\phi}}{D_w}e^{iw_x(L+d)} + D\frac{\eta c_w e^{-i\eta(\pi-\phi)}}{D_w}e^{-iw_x(L+d)} = E\frac{\eta c_q e^{-i\eta\varphi}}{D_q}e^{iq_x(L+d)} + F\frac{\eta c_q e^{-i\eta(\pi-\varphi)}}{D_q}e^{-iq_x(L+d)}, \tag{A12}$$

$$C\frac{b_w}{D_w}e^{iw_x(L+d)} + D\frac{b_w}{D_w}e^{-iw_x(L+d)} = E\frac{b_q}{D_q}e^{iq_x(L+d)} + F\frac{b_q}{D_q}e^{-iq_x(L+d)}. \tag{A13}$$

Finally, at $x = L + d + L$, $\Psi_{\rm IV}(2L+d) = \Psi_{\rm V}(2L+d)$ and we obtain

$$E\frac{\eta c_q e^{-i\eta\varphi}}{D_q}e^{iq_x(2L+d)} + F\frac{\eta c_q e^{-i\eta(\pi-\varphi)}}{D_q}e^{-iq_x(2L+d)} = t_{\eta,S_z}\frac{\eta c_k e^{-i\eta\theta}}{D_k}e^{ik_x(2L+d)}, \tag{A14}$$

$$E\frac{b_q}{D_q}e^{iq_x(2L+d)} + F\frac{b_q}{D_q}e^{-iq_x(2L+d)} = t_{\eta,S_z}\frac{b_k}{D_k}e^{ik_x(2L+d)}. \tag{A15}$$

The $r^{\rm Double}_{\eta,S_z}$ and $t^{\rm Double}_{\eta,S_z}$ coefficients are obtained by solving the systems of equations defined by Eqs. A8– A15, resulting in the following expression for the transmission coefficient:

$$t^{\rm Double}_{\eta,S_z} = \frac{16e^{-2ik_x L}e^{-ik_x d}\cos(\varphi)^2\cos(\phi)\cos(\theta)}{\xi}, \tag{A16}$$

with the denominator ξ given by

$$\xi = F_1 + \left(\frac{c_k b_w}{c_w b_k} + \frac{c_w b_k}{c_k b_w}\right)F_2 + \left(\frac{c_k b_q}{c_q b_k} + \frac{c_q b_k}{c_k b_q}\right)F_3 + \left(\frac{c_q b_w}{c_w b_q} + \frac{c_w b_q}{c_q b_w}\right)F_4 + \left(\frac{c_k c_w b_q^2}{c_q^2 b_k b_w} + \frac{c_q^2 b_k b_w}{c_k c_w b_q^2}\right)F_5, \tag{A17}$$

where the functions F_i are defined as

$$F_1 = -8i\sin(w_x d)\cos(\theta+\phi) + 8i\sin(w_x d)\cos(\theta-\phi) + 4e^{iw_x d}\cos(2q_x L)\cos(\theta+\phi) + 4e^{-iw_x d}\cos(2q_x L)\cos(\theta-\phi) + 2e^{-iw_x d}e^{-2iq_x L}\cos(\theta+\phi+2\varphi) + 2e^{iw_x d}e^{-2iq_x L}\cos(\theta-\phi+2\varphi) + 2e^{-iw_x d}e^{2iq_x L}\cos(\theta+\phi-2\varphi) + 2e^{iw_x d}e^{2iq_x L}\cos(\theta-\phi-2\varphi), \quad \text{(A18)}$$

$$F_2 = -4i\sin(w_x d)\left[\cos(2Lq_x) + \cos(2\varphi)\right], \quad \text{(A19)}$$

$$F_3 = -4i\left[\sin(w_x d) + \sin(2q_x L - w_x d)\right]\cos(\varphi-\phi) + 4i\left[\sin(w_x d) - \sin(2q_x L + w_x d)\right]\cos(\varphi+\phi), \quad \text{(A20)}$$

$$F_4 = -8\sin(w_x d)\, e^{iq_x L}\sin(q_x L)\cos(\theta-\varphi) - 8\sin(w_x d)\, e^{-iq_x L}\sin(q_x L)\cos(\theta+\varphi), \quad \text{(A21)}$$

and

$$F_5 = 8i\sin(w_x d)\sin(q_x L)^2. \quad \text{(A22)}$$

For the single-barrier heterostructure, the wave functions for zones III and IV must be neglected and d must be set equal to zero. A similar equation system is then obtained. The transmission coefficient of the single barrier, $t^{\text{Single}}_{\eta,S_z}$, is analytically determined and is given by Eqs. (6) and (7).

[1] T. Norden, C. Zhao, P. Zhang, R. Sabirianov, A. Petrou, and H. Zeng, Giant valley splitting in monolayer WS_2 by magnetic proximity effect, Nat. Commun. **10**, 4163 (2019).

[2] J. Qi, X. Li, Q. Niu, and J. Feng, Giant and tunable valley degeneracy splitting in $MoTe_2$, Phys. Rev. B **92**, 121403 (2015).

[3] M. Tahir, P. M. Krstajić, and P. Vasilopoulos, Magnetic and electric control of spin- and valley-polarized transport across tunnel junctions on monolayer WSe_2, Phys. Rev. B **95**, 235402 (2017).

[4] H. Li, J. Shao, D. Yao, and G. Yang, Gate-voltage-controlled spin and valley polarization transport in a normal/ferromagnetic/normal MoS_2 junction, ACS Appl. Mater. Interfaces **6**, 1759 (2014).

[5] K. S. Novoselov, A. Mishchenko, A. Carvalho, and A. H. Castro Neto, 2D materials and van der Waals heterostructures, Science **353**, 6298 (2016).

[6] Q. H. Wang, K. Kalantar-Zadeh, A. Kis, J. N. Coleman, and M. S. Strano, Electronics and optoelectronics of two-dimensional transition metal dichalcogenides, Nat. Nanotechnol. **7**, 699 (2012).

[7] S. Manzeli, D. Ovchinnikov, D. Pasquier, O. V. Yazyev, and A. Kis, 2D transition metal dichalcogenides, Nat. Rev. Mater. **2**, 17033 (2017), and *all references therein.*

[8] M. Chhowalla, H. S. Shin, G. Eda, L.-J. Li, K. P. Loh, and H. Zhang, The chemistry of two-dimensional layered transition metal dichalcogenide nanosheets, Nat. Chem. **5**, 263 (2013).

[9] Z. Wang, L. Zhao, K. F. Mak, and J. Shan, Probing the spin-polarized electronic band structure in monolayer transition metal dichalcogenides by optical spectroscopy, Nano Lett. **17**, 740 (2017).

[10] C. Zhang, Y. Chen, J. K. Huang, X. Wu, L. J. Li, W. Yao, J. Tersoff, and C. K. Shih, Visualizing band offsets and edge states in bilayer–monolayer transition metal dichalcogenides lateral heterojunction, Nat. Commun. **7**, 10349 (2016).

[11] X. Xu, W. Yao, D. Xiao, and T. F. Heinz, Spin and pseudospins in layered transition metal dichalcogenides, Nat. Phys. **10**, 343 (2014).

[12] X. Qian, J. Liu, L. Fu, and J. Li, Quantum spin Hall effect in two-dimensional transition metal dichalcogenides, Science **346**, 1344 (2014).

[13] G. B. Liu, W. Y. Shan, Y. Yao, W. Yao, and D. Xiao, Three-band tight-binding model for monolayers of group-VIB transition metal dichalcogenides, Phys. Rev. B **88**, 085433 (2013).

[14] A. J. Pearce, E. Mariani, and G. Burkard, Tight-binding approach to strain and curvature in monolayer transition-metal dichalcogenides, Phys. Rev. B **94**, 155416 (2016).

[15] D. Xiao, G. B. Liu, W. Feng, X. Xu, and W. Yao, Coupled Spin and Valley Physics in Monolayers of MoS_2 and Other Group-VI Dichalcogenides, Phys. Rev. Lett. **108**, 196802 (2012).

[16] H. Li, J. Shao, D. Yao, and G. Yang, Gate-voltage-controlled spin and valley polarization transport in a normal/ferromagnetic/normal MoS_2 junction, ACS Appl. Mater. Interfaces **6**, 1759 (2014).

[17] M. Tahir, P. M. Krstajic, and P. Vasilopoulos, Zeeman- and electric-field control of spin- and valley-polarized transport through biased magnetic junctions on WSe_2, EPL **118**, 17001 (2017).

[18] Y. Ominato, J. Fujimoto, and M. Matsuo, Valley-Dependent Spin Transport in Monolayer Transition-Metal Dichalcogenides, Phys. Rev. Lett. **124**, 166803 (2020).

[19] W. Choi, N. Choudhary, G. H. Han, J. Park, D. Akinwande, and Y. H. Lee, Recent development of two-dimensional transition mdetal dichalcogenides and their applications, Mater. Today **20**, 116 (2017).

[20] C. Zhou, Y Zhao, s. Raju, Y. Wang, Z. Lin, M. Chan, and Y. Chai, Carrier type control of WSe_2 field-effect transistors by thickness modulation and MoO_3 layer doping, Adv. Funct. Mater. **26**, 4223 (2016).

[21] H. Tian, M. L. Chin, S. Najmaei, Q. Guo, F. Xia, H. Wang, and M. Dubey, Optoelectronic devices based on two-dimensional transition metal dichalcogenides, Nano Res. **9**, 1543 (2016).

[22] K. F. Mak and J. Shan, Photonics and optoelectronics of 2D semiconductor transition metal dichalcogenides, Nat. Photonics **10**, 216 (2016).

[23] J. H. Yu, H. R. Lee, S. S. Hong, D. Kong, H.-W. Lee, H. Wang, F. Xiong, S. Wang, and Y. Cui, Vertical heterostructure of two-dimensional MoS_2 and WSe_2 with vertically aligned layers, Nano Lett. **15**, 1031 (2015).

[24] H. Li, Z. Yin, Q. He, H. Li, X. Huang, G. Lu, D. W. F. Fam, A. I. Y. Tok, Q. Zhang, and H. Zhang, Fabrication of single- and multilayer MoS_2 film-based field-effect transistors for sensing NO at room temperature, Small **8**, 63 (2012).

[25] A. J. Molina-Mendoza, M. Paur, and T. Mueller, Non-volatile programmable WSe_2 photodetector, Adv. Opt. Mater. **8**, 2000417 (2020).

[26] R. Lv, J. A. Robinson, R. E. Schaak, D. Sun, Y. Sun, T. E. Mallouk, and M. Terrones, Transition metal dichalcogenides and beyond: Synthesis, properties, and applications of single- and few-layer nanosheets, Acc. Chem. Res. **48**, 56 (2015).

[27] H. R Gutiérrez, N Perea-López, A. L. Elías, A. Berkdemir, B. Wang, R. Lv, F. López-Urías, V. Crespi, H. Terrones, and M. Terrones, Extraordinary room-temperature photoluminescence in triangular WS monolayers, Nano Lett. **13**, 3447 (2013).

[28] G. Aivazian, Z. Gong, A. M Jones, R.-L. Hu, J. Yan, D. G. Mandrus, C. Zhang, D. Cobden, W. Yao, and X. Xu, Magnetic control of valley pseudospin in monolayer WSe_2, Nat. Phys. **11**, 148 (2015).

[29] Y. Liu, Y. Gao, S. zhang, J. He, J. Yu, and Z. Liu, Valleytronics in transition metal dichalcogenides materials, Nano Res. **12**, 2695 (2019).

[30] B. T. Zhou, K. Taguchi, Y. Kawaguchi, Y. Tanaka, and K. T. Law, Spin-orbit coupling induced valley Hall efects in transition-metal dichalcogenides, Commun. Phys. **2**, 26 (2019).

[31] M. Buttiker, H. Thomas, and A. Pretre, Current partition in multiprobe conductors in the presence of slowly oscillating external potentials, Z. Phys. B: Condens. Matter **94**, 133 (1994).

[32] G. Platero and R. Aguado, Photon-assisted transport in semiconductor nanostructures, Phys. Rep. **395**, 1 (2004).

[33] S. Kholer, J. Lehmann, and P. Haennggi, Driven quantum transport on the nanoscale, Phys. Rep. **406**, 379 (2005).

[34] B. L. Altshuler and L. I. Glazman, Pumping electrons, Science **283**, 1864 (1999).

[35] C. Kocabas, H.-S. Kim, T. Banks, J. A. Rogers, A. A. Pesetski, J. E. Baumgardner, S. V. Krishnaswamy, H. Zhang, *et al.*, Radio frequency analog electronics based on carbon nanotube transistors, PNAS **105**, 1405 (2008).

[36] D. Zambrano, L. Rosales, A. Latgé, M. Pacheco, and P. A. Orellana, Photon-assisted transport in bilayer graphene flakes, Phys. Rev. B **95**, 035412 (2017).

[37] C. G. Rocha, L. E. F. Foa Torres, and G. Cuniberti, AC transport in graphene-based Fabry-Pérot devices, Phys. Rev. B **81**, 115435 (2010).

[38] C. Rocha, M. Pacheco, L. E. F. Foa Torres, G. Cuniberti, and A. Latgé, Transport response of carbon-based resonant cavities under time-dependent potential and nagnetic fields, EPL **94**, 47002 (2011).

[39] L. E. F. Foa Torres, H. L. Calvo, C. G. Rocha, and G. Cuniberti, Enhancing single-parameter quantum charge pumping in carbon-based devices, Appl. Phys. Lett. **99**, 092102 (2011).

[40] G. Usaj, P. M. Perez Piskunow, L. E. F. Foa Torres, and C. A. Balseiro, Irradiated graphene as a tunable Floquet topological insulator, Phys. Rev. B **90**, 115423 (2014).

[41] Z. Yin, H. Li, H. Li, l. jiang, y. Shi, G. Lu, Q. Zhang, X. Chen, and H. Zhang, Single-layer MoS_2 phototransistors, ACS Nano. **6**, 74 (2012).

[42] K. Roy, M. Padmanabhan, S. Goswami, T. P. Sai, G. Ramalingam, S. Raghavan, and A. Ghosh, Graphene-MoS_2 hybrid structures for multifunctional photoresponsive memory devices, Nat. Nanotech. **8**, 826 (2013).

[43] R. Cheng, D. Li, H. Zhou, C. Wang, A. Tin, S. Jiang, Y. Liu, Y. Chen, Y. Huang, and X. Duan, Electroluminescence and photocurrent generation from atomically sharp WSe_2/MoS_2 heterojunction *p-n* diodes, Nano Lett. **14**, 5590 (2014).

[44] X.-J. Hao, R. -Y. Yuan, T. Ji, and Y. Guo, Switch effect for spin-valley electrons in monolayer WSe_2 structures subjected to optical field and Fermi velocity barrier, J. Appl. Phys. **128**, 154303 (2020).

[45] P. K. Tien and J. R. Gordon, Multiphoton process observed in the interaction of microwave fields with the tunneling between superconductor films, Phys. Rev. **129**, 2 (1963).

[46] S. Fathipour, P. Paletti, S. K. Fullerton-Shirey, and A. C. Seabaugh, Electric-double-layer *p-i-n* junctions in WSe_2, Sci. Rep. **10**, 12890 (2020).

[47] P. A. Orellana, L. Rosales, L. Chico, and M. Pacheco, Spin-polarized electrons in bilayer graphene ribbons, J. Appl. Phys. **113**, 21 (2013).